International Journal of Fatigue 210 (2026) 109659

Contents lists available at ScienceDirect

International Journal of Fatigue

journal homepage: www.elsevier.com/locate/ijfatigue

# A unified probabilistic defect-based fatigue modelling approach to account for surface and bulk defects in additively manufactured Ti-6Al-4V alloys and defect characterisation☆

Enrico Salvati [a,*], Marco Pelegatti [a], Marco Petruzzi [b], Alessandro Tognan [a], Emanuele Avoledo [a], Federico Milan [a], Francesco De Bona [a], Niki Picco [a], Francesco Sordetti [a], Alex Lanzutti [a], Michele Pressacco [b], Riccardo Toninato [b]

[a] Polytechnic Department of Engineering and Architecture, University of Udine, Via delle Scienze 206, Udine 33100, Italy
[b] LimaCorporate Spa, part of Enovis Corporation, Via Nazionale 52, Villanova, San Daniele del Friuli, 33038, Italy

ARTICLE INFO

*Keywords:*
Defect-based
Fracture Mechanics
Ti-6Al-4V
Fatigue
Roughness
Additive manufacturing

ABSTRACT

Additively manufactured metals are often affected by material inhomogeneities across multiple length scales. Geometrical inhomogeneities, as well as non-metallic inclusions — commonly referred to as defects — can significantly impair the fatigue performance of the fabricated material, especially in the absence of further post-processing. Therefore, accounting for these defects is essential for a proper assessment of the material's structural integrity.

Fracture Mechanics-based approaches have proven effective in addressing bulk and sub-surface defects; however, a consensus has yet to be reached on the most effective method for addressing surface geometrical inhomogeneities (e.g., surface roughness).

This work presents the effectiveness of a generalised defect-based model capable of accounting for bulk, sub-surface, and surface defect (roughness) effects on the fatigue endurance limit. The proposed model is calibrated on a detailed experimental fatigue characterisation study of a Ti-6Al-4V alloy manufactured through two different techniques, i.e., Electron Beam Melting (EBM) and Selective Laser Melting (SLM). To achieve varied defect characteristics and quantitatively assess their influence on fatigue, the additively manufactured materials were subjected to different combinations of post-processing (e.g., Hot Isostatic Pressing, Vacuum Heat Treatment). Defect distributions were investigated using the non-destructive lab-based Computed Tomography (CT), and further data analysis was conducted by exploiting the Extreme Value Statistics (EVS) theory.

The approach was effective across all studied material conditions, providing a probabilistic assessment of fatigue failure performance.

## 1. Introduction

Additive manufacturing (AM) has revolutionised the fabrication of metallic mechanical components, offering unprecedented design flexibility, reduced material waste, and the ability to create complex geometries that would be difficult or impossible to achieve using conventional manufacturing methods [1]. However, despite its many advantages, AM metals exhibit unique material challenges, primarily related to the presence of microstructural anomalies that arise during the fabrication process, often referred to as defects [2]. These defects, which manifest across multiple length scales, can significantly impact the mechanical performance of AM components, particularly their fatigue resistance, which is crucial for structural applications [3].

Defects include a wide range of – often unwanted – features, such as non-metallic inclusions, gas porosity, lack of fusion voids, and anomalous asperities related to surface roughness. These defects act as stress concentrators, reducing the material's ability to withstand cyclic loading and increasing the likelihood of premature fatigue failure. While extensive research has been conducted on the role of bulk and sub-surface defects in fatigue behaviour, the effect of surface roughness remains a complex and unresolved issue. The surface topography of AM

☆ This article is part of a special issue entitled: 'FDMD 5' published in International Journal of Fatigue.

* Corresponding author.
*E-mail address:* enrico.salvati@uniud.it (E. Salvati).

https://doi.org/10.1016/j.ijfatigue.2026.109659
Received 16 January 2026; Received in revised form 30 March 2026; Accepted 31 March 2026
Available online 2 April 2026

**Nomenclature**

| | |
|---|---|
| AM | Additive manufacturing |
| CT | Computed Tomography |
| EBM | Electron Beam Melting |
| EH | El Haddad |
| EVS | Extreme Value Statistics |
| HIP | Hot Isostatic Pressing |
| LEMF | Linear Elastic Fracture Mechanics |
| N | As-built specimen |
| NT | Machined specimen |
| SIF | Stress Intensity Factor |
| SLM | Selective Laser Melting |
| T | Hipped specimen |
| VHT | Vacuum Heat Treatment |

components is inherently rough due to the layer-by-layer nature of the process and specific powder characteristics. Traditionally, fatigue life prediction requires multiple design curves based on specific processing techniques and post-processing treatments. However, such an approach can be cumbersome and limit the standardisation of AM component design.

Linear Elastic Fracture Mechanics (LEFM) provides a robust theoretical foundation for understanding the fatigue crack propagation criteria in defect-laden materials, thanks to the comprehensive contribution of Murakami [4]. By considering defects as initial cracks, LEFM enables a physics-based approach to quantifying their influence on fatigue life. Existing fracture mechanics-based approaches have been effective in modelling bulk [5,6] or sub-surface defects [7–9] or both [10–12], including more advanced Machine Learning methods [13–16] or even advanced hybrid methods relying on the physics-informed ML paradigms [17–20]. Nevertheless, a comprehensive and unified framework capable of simultaneously accounting for all defect types—including surface roughness—has yet to be established. In fact, the cited studies addressed the roles of bulk and surface defects separately, without, for example, validating a single Kitagawa diagram for a specific material that is effective across all defect types. Moreover, utilising LEFM in conjunction with a probabilistic framework allows for a more reliable assessment of fatigue failure, bridging the gap between experimental fatigue data and predictive modelling [21,22].

To address this critical research gap, the present study introduces a probabilistic defect-based fatigue modelling approach that systematically incorporates bulk, sub-surface, and surface defects in the assessment of the fatigue endurance limit. This model is developed based on an extensive experimental fatigue characterisation study performed by the authors for a Ti-6Al-4V alloy fabricated using two AM techniques: Electron Beam Melting (EBM) and Selective Laser Melting (SLM). To systematically assess the influence of defects on fatigue performance and to calibrate the model over a wide range of defect severities, the materials were subjected to various post-processing treatments, including Hot Isostatic Pressing (HIP) and in-vacuum Heat Treatment (VHT). Following, a single El Haddad (EH) design curve for each additive manufacturing process that accounts for different material processing conditions is evaluated by leveraging a probabilistic framework to provide a richer assessment of fatigue failure in AM Ti-6Al-4V alloys.

For prediction purposes, the probabilistic fatigue design curve established in this work can be effectively exploited if the statistical distribution of the defects present in the investigated material is known. To provide the reader with this information, the examined material batches were also analysed using Computer Tomography (CT) where possible. Following the CT-retrieved distributions, alongside the statistically significant data about defects obtained by post-mortem fractography analysis of tested samples, were individually analysed by exploiting Extreme Value Statistics (EVS) theory [23,24].

**Table 1**
Considered material conditions and sample ID.

| ID | Manufacturing Route | | | Number of specimens tested |
|---|---|---|---|---|
| | Additive Manufacturing Technology | Surface finishing | Thermo-mechanical treatment | |
| EBM-N | EBM | As-built | N/A | 19 |
| EBM-NT | EBM | Machined | N/A | 20 |
| EBM-T | EBM | Machined | HIP | 12 |
| SLM-N | SLM | As-built | VHT | 15 |
| SLM-NT | SLM | Machined | VHT | 21 |
| SLM-T | SLM | Machined | VHT + HIP | 13 |

## 2. Materials and methods

Two different additive manufacturing technologies were employed for the production of Ti-6Al-4V alloy samples for fatigue characterisation, i.e., EBM and SLM, according to the experimental results previously presented by the authors in a dedicated paper [25]. Dog-bone cylindrical specimens with a 16.5 mm gauge length and 5.5 mm diameter were printed in the vertical direction using optimised process parameters. With the aim of achieving a wide range of material conditions for each manufacturing technology, three different batches of samples were produced under different post-manufacturing processes: as-built (N), machined (NT) and machined followed by HIP treatment (T). Additionally, the SLMed samples were always subjected to VHT as the primary heat treatment.

Table 1 summarises the sample conditions considered in the present work.

### 2.1. Fatigue data

Fatigue tests were carried out to assess the endurance limit at $10^7$ cycles and the fatigue lifetime curve in the high cycle fatigue regime. A constant stress range was imposed during the test with a stress ratio of R = 0.1. The number of specimens tested for each condition is reported in Table 1. Please note that some runout specimens were retested at higher stress levels, as will be mentioned in **Section 4.2**. More details on the experimental procedure are reported in a dedicated publication by the authors [25]. Without loss of generality, the applied stress range can be normalised by the Vickers' hardness. This normalisation mainly serves the purpose of not disclosing sensitive data, such as the fatigue endurance limit of each batch of material. Such a normalisation does not limit the interpretability and applicability of the approach to other classes of metallic materials. Indeed, the fatigue properties of many metallic materials are somehow directly proportional to the material's hardness, a valid hypothesis for several metallic materials [4,26,27]. The normalised stress range is:

$$\chi = \frac{\Delta\sigma \bullet 100}{\mathrm{HV}_{EBM}} \tag{1}$$

where $\Delta\sigma\,[MPa]$ is the applied stress range and $\mathrm{HV}_{EBM}\left[kg_f/mm^2\right]$ is the Vickers' hardness of the EBM-T batch. The unit of $\chi$ turns out $\left[N/kg_f\right]$. In the present work, the normalisation of the samples is done using the hardness values of the T conditions for the EBM technology.

According to the proposed normalisation, Fig. 1 reports the S-N diagrams and respective reference curves for all the considered material

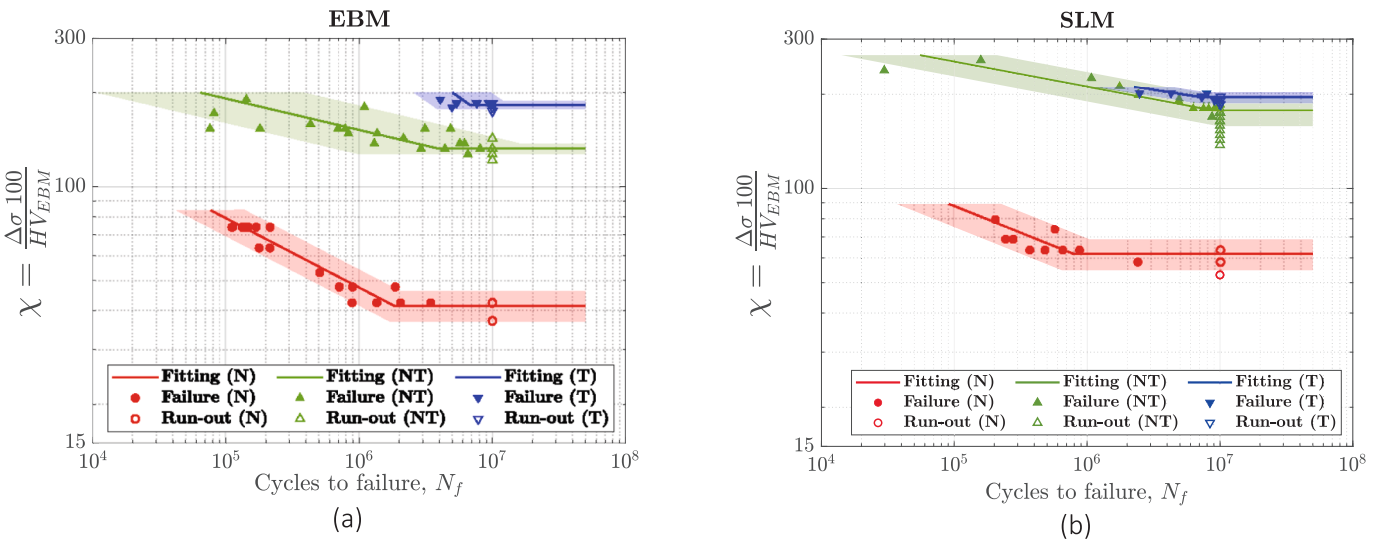


**Fig. 1.** Normalised fatigue experimental data and fitted curves. (a) EBM and (b) SLM.

batches. The horizontal line of the fatigue endurance limit was estimated using the staircase procedure, whereas the finite life curve corresponds to the fitted Basquin model. The intersection of the two lines provides the knee point in the S-N curve. For both AM technologies, the as-built condition (N) exhibits a lower endurance limit, consistent with other literature studies [28–31]. This behaviour is related to the significant detrimental role of surface defects associated with the roughness, as will be discussed in **Sections 4.2 and 3.2**. Interestingly, the HIP treatment provides a less pronounced improvement in the fatigue endurance limit of machined SLM specimens compared to the case of the machined EBM batch. Although a more in-depth discussion on the cause of this effect is shown in **Sections 4.2 and 3.1**, the origin of this outcome is related to the different defect sizes in EBM and SLM batches, with the latter already showing smaller defect sizes.

### 2.2. Defect analysis approaches

The analysis of internal (bulk) and surface geometrical inhomogeneities plays a pivotal role in the proposed model. To comprehensively characterise these features statistically, relatively large datasets are required. Concerning bulk inhomogeneities, which are regarded as defects, two approaches were pursued to tackle this problem, respectively regarded as destructive and non-destructive techniques.

The former was pursued through the exploitation of fatigued samples' fracture surface analysis, which was probed through Scanning Electron Microscopy (SEM) – this allowed for a precise quantification of $\sqrt{\text{area}}$ of the defects that triggered fatigue failure, i.e. killer defects. Assuming that defects lie either far from the sample free-surface or close enough to the free-surface, killer defects can be considered as the defects with the maximum $\sqrt{\text{area}}$ size for each specimen, meaning that the largest defect size is responsible for fatigue crack nucleation and further propagation. For defects very close to the surface, the measured area includes a strip of material between the defect and the specimen's edge surface. Similarly, for defects close to each other, the area size encloses the outlines of all defects. Similarly, a fractographic analysis was performed to characterise the morphological traits of killer defects lying on the sample free surface – mostly occurring in the as-built sample conditions (EBM-N and SLM-N). The way this information is employed in the establishment of the predictive tool will be discussed later.

On the other hand, non-destructive assessment of bulk defects can be attained through CT analysis [21,32,33]. In the current study, the software VGStudio Max® was used to reconstruct the CT analyses and to perform the pore analyses. Specifically, defect identification was carried out through the VGEasyPore® software package. Obviously, this approach has the advantage of analysing a large quantity of "hidden" defects without compromising its integrity. Nevertheless, it is not able to provide direct information neither on the killer defect nor the most critical one, unless fracture mechanics concepts are introduced. On top of that, CT analysis may suffer significant uncertainties, especially when using lab-based CT equipment [34,35].

Non-destructive characterisation of surface roughness was performed using optical microscopy. For the reasons that will be detailed later, amongst the surface roughness descriptors, the maximum pit depth parameter, $S_v$, was evaluated on several sampling surfaces to draw a statistical distribution.

The size of killer defects will be used to estimate the EH model of NT and T batches, where each killer defect is assigned to the corresponding specimen. In the case of as-built batches (EBM-N and SLM-N), the parameter $S_v$ is exploited instead of the killer defect size due to the high uncertainty in determining a unique value from fractographic analysis. The challenge of clearly identifying the size of killer defects associated with surface roughness is well-known in the literature [7,29,36]. Furthermore, in the present work, killer defect sizes almost always underestimate the defect criticality compared to the maximum expected parameter $S_v$ in the specimen surface obtained by surface roughness measurements.

For both destructive and non-destructive methods, statistical information can be gathered regarding the distribution of defects, or killer defects. This information can provide quantitative insights into the probability of the occurrence of a certain defect size. Therefore, a probabilistic evaluation of the fatigue performance of a defect-laden material or component can be pursued.

#### 2.2.1. Extreme value statistics

The global size distribution of defects provides useful information about the quality of the manufacturing process. However, only the maximum defect sizes of the defects presented in the component play a role in the fatigue failure. In fact, the main fatigue crack that leads to fracture always nucleates at the most detrimental defect, which is usually the one with the largest size, unless relevant intra- and intergranular residual stress are present in the material.

Therefore, it is relevant to focus on the upper tail of the size distribution of the defects instead of considering the whole distribution. From that perspective, the fatigue phenomenon is governed by the extreme values of the defect size distribution. A common way to include the

influence of the defect size on the fatigue strength is to describe the maximum defect sizes by means of the statistics of extremes [4,24,37]. Then, the descriptors of the statistical distribution can be included in the fatigue assessment of a component by an appropriate mathematical procedure and considering the fatigue strength model (e.g., EH model) [38,39].

One way to model the upper tail of the defect size distribution is to consider the maximum values in sufficiently large volumes (those including enough defects). In that case, the distribution of the maximum value in the "large" volume is a random variable that tends to follow (asymptotically) the family of the Generalised Extreme Value distributions [23]. Considering the defect size as the random variable of interest, it is experimentally proven that, amongst the Generalised Extreme Value distributions, the Gumbel distribution can accurately describe the statistical distribution of the maximum defect size in a control volume [24].

The cumulative distribution function of the Gumbel distribution is expressed as follows:

$$F_{V_0}\left(\sqrt{area}_{max}\right) = \exp\left(-\exp\left(-\frac{\sqrt{area}_{max}-\mu}{\sigma}\right)\right) \tag{2}$$

where $\mu$ and $\sigma$ are the location and scale parameters. The considered random variable, $\sqrt{area}_{max}$, in Eq.(2) is the maximum projected area $\sqrt{area}$ in the chosen control volume $V_0$.

From Eq.(2) follows that the maximum defect size associated with the percentile p −th is:

$$\sqrt{area}_{max}(p) = \mu + \sigma(-\ln(-\ln p)) \tag{3}$$

where $F_{V_0}$ was changed to p, which assumes the same meaning, i.e. probability that $\sqrt{area}_{max}$ takes on a value less than or equal to a specific value.

From a practical point of view, the location and scale parameters can be estimated from an empirical distribution of the maximum defect size in a control volume. This empirical distribution can be obtained by adopting a sampling strategy called block maxima.

First, the size of the control volume $V_0$ and, consequently, the number of volumes $n_V$ must be decided (if we consider a fixed inspected volume). Then, the maximum defect size is obtained for each volume, leading to $n_V$ local maxima. At this point, these values are sorted in ascending order and an empirical cumulative probability is assigned at each defect size:

$$F_{V_0}\left(\sqrt{area}_i\right) = \frac{i}{n_V+1} \tag{4}$$

In Eq. (4) and in the equations that follow, the symbol $\sqrt{area}$ replaces that of $\sqrt{area}_{max}$ for the sake of brevity.

By plotting the experimental data in a graph $-\ln(-\ln F)$ versus $\sqrt{area}$ is possible to verify if the data follows a linear trend, as predicted by the Gumbel distribution. Here, to simplify the notation, F is used instead of $F_{V_0}$, but both refer to the cumulative distribution function.

Finally, the location and scale parameters are estimated using the maximum likelihood method [40]. The scale parameter must be obtained first from the following equation:

$$\overline{\sqrt{area}} - \frac{\sum_{i=1}^{n_V}\sqrt{area}_i \exp(-\sqrt{area}_i/\hat{\sigma}_{ML})}{\sum_{i=1}^{n_V}\exp(-\sqrt{area}_i/\hat{\sigma}_{ML})} - \hat{\sigma}_{ML} = 0 \tag{5}$$

using an iterative procedure. The symbol $\overline{\sqrt{area}}$ indicates the sample mean of the defect size values and $\hat{\sigma}_{ML}$ is the maximum likelihood estimator of the scale parameter.

Then, the location parameter can be obtained directly from:

$$\hat{\mu}_{ML} = -\hat{\sigma}_{ML}\ln\left(\frac{1}{n_V}\sum_{i=1}^{n_V}\exp(-\sqrt{area}_i/\hat{\sigma}_{ML})\right) \tag{6}$$

where $\hat{\mu}_{ML}$ is the maximum likelihood estimator of the location parameter.

Other two methods to estimate the parameters of the Gumbel distribution are the least-squares (linear regression) and moments methods. As demonstrated by Beretta and Murakami, the most efficient method is the maximum likelihood method [41].

The size of the control volume is usually smaller than the size of the engineering components, and the location and scale parameters estimated before cannot directly be used. However, the statistical distribution of the maximum defect in a larger volume $V_c = TV_0$ can be obtained again by a Gumbel distribution, where the location and scale parameters are now:

$$\begin{cases} \mu_{V_c} = \mu + \sigma \ln T \\ \sigma_{V_c} = \sigma \end{cases} \tag{7}$$

This result is obtained by using the concept of the return period T. In a few words, if the considered volume is T-times the control volume $V_0$, for which the Gumbel distribution has been estimated, the probability of having a maximum defect size lower than a critical value ($\sqrt{area}_{cr}$) in the volume $V_c = TV_0$ is equal to the probability that T volumes of size $V_0$ have simultaneously a maximum defect size lower than a critical value:

$$\Pr\left\{\sqrt{area}_{max,V_c} < \sqrt{area}_{cr}\right\} = \left[\Pr\left\{\sqrt{area}_{max,V_o} < \sqrt{area}_{cr}\right\}\right]^{T=V_c/V_0}$$

$$\rightarrow F_{V_c}\left(\sqrt{area}_{max}\right) = \left[F_{V_0}\left(\sqrt{area}_{max}\right)\right]^{T=V_c/V_0} \tag{8}$$

Confidence bands can be obtained for each estimated quantile given by Eq.(3) and the estimated parameters. The upper and lower limits of the $\gamma$% confidence band for a given quantile are [41,42]:

$$\begin{matrix}\sqrt{area}_{\gamma,+}(p) \\ \sqrt{area}_{\gamma,-}(p)\end{matrix} = \sqrt{area}(p) \pm K_\gamma \frac{\hat{\sigma}_{ML}}{\sqrt{n_V}}\sqrt{1.11+0.52y+0.61y^2} \tag{9}$$

where $y = -\ln(-\ln F)$ and $K_\gamma$ is the $(1+\gamma)/2$ standard Gaussian percentile.

The EVS analysis outlined above can be applied to both bulk and surface defects, where the appropriate defect size must be adopted. In the present work, $\sqrt{area}$ evaluated from CT scans and fractography is adopted to assess the EVS for bulk defects, whereas an equivalent $\sqrt{area}_{eq}$ is defined starting from $S_v$ for non-destructive analysis of surface roughness.

### 2.3. Fatigue modelling approach

In the present work, the model proposed by El Haddad (EH) is employed to establish a fatigue failure criterion at a predefined runout threshold $N^*$ in terms of the number of cycles. Such a model is of a semi-empirical nature, based on LEFM, whereby practitioners can outline the fatigue endurance limit of defective metallic materials [43].

In order to apply the EH model to defective metallic materials, defects are regarded as cracks and assigned a representative crack length. Murakami's approach is pursued for the purpose of the present investigation, i.e. the representative crack length corresponds to the square root of the projected area of the defects over the plane normal to the loading direction, namely $\sqrt{area}$ [1]. Accordingly, the EH curve is analytically described by [44]:

$$\Delta\sigma = \Delta\sigma_w\sqrt{\frac{\sqrt{area}_0}{\sqrt{area}+\sqrt{area}_0}} \tag{10}$$

where $\Delta\sigma_w$ is the fatigue endurance limit of the defect-free material and $\sqrt{area}_0$ is the EH critical length. The latter can be easily interpreted by referring to Kitagawa's diagram, which $\sqrt{area}_0$ is the critical defect size, above which the presence of a defect plays a role in the integrity of the material. Contrarily, the presence of defects smaller than these critical

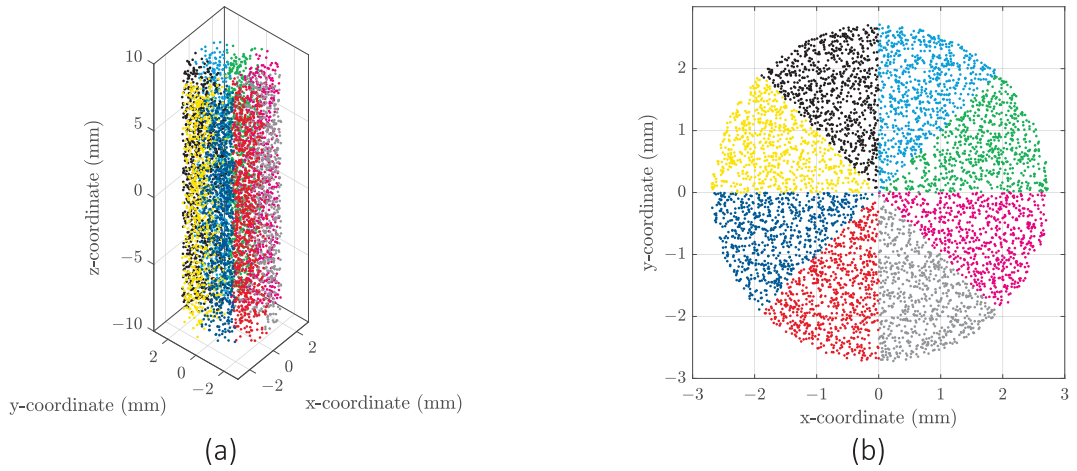


**Fig. 2.** Block maxima sampling strategy applied to the machined specimen NT1-4: (a) global view of the considered CT scanned volume and (b) top view of the specimen to highlight the division into the sub-volumes identified by different colours (each point represents the centroid of a defect).

dimensions does not lead to any fatigue crack propagation. Therefore, the parameter $\sqrt{\text{area}_0}$ is essential in describing the fatigue properties of defect-laden materials:

$$\sqrt{\text{area}_0} = \frac{1}{\pi}\left(\frac{\Delta K_{th,lc}}{Y\Delta\sigma_w}\right)^2 \tag{11}$$

in which, $\Delta K_{th,lc}$ is the fatigue Stress Intensity Factor (SIF) range threshold for long cracks, and Y is a factor that depends upon the distance between the centroid of the defect and free-surface of the specimen. In the present work, the critical flaw size, $\sqrt{\text{area}_0}$, is later identified univocally through a specific algorithm (i.e. B-FADE) previously presented by some of the present authors [22,45], referring to the EH's critical defect size; relying on the sole knowledge of killer defect sizes and whether the sample failed or not at a given $N^*$. This is necessary because the defect-free fatigue endurance limit, $\Delta\sigma_w$, is nearly impossible to obtain due to the intrinsic presence of defects in the probed material.

The value of $\sqrt{\text{area}_0}_{EBM}$, identified through the employment of B-FADE for the EBM material condition, will be used to normalise defect sizes, and this parameter will not be disclosed once identified.

Importantly, B-FADE allows for the introduction of statistical knowledge of $\Delta K_{th,lc}$ to make the EH curve identification more robust and reliable. Following, details about the evaluation of the fatigue SIF thresholds are provided.

#### 2.3.1. Fatigue SIF thresholds determination

The knowledge of the fatigue SIF range threshold is a fundamental fatigue characteristic that allows a predictive model to establish whether a long crack propagates when subjected to repeated loadings. Given that the approach proposed herein is based on the fundamental assumption of material defects being cracks, according to Murakami [4], this parameter is an essential requirement.

As concerns the EBM samples, fatigue crack growth tests were carried out to characterise $\Delta K_{th,lc}$ of the EBM-NT batch. Three samples were tested according to the standard ASTM E647-24, meaning that the surface finishing was also prepared according to the standard.

As far as the SLM material condition is concerned, the fatigue crack growth threshold was not experimentally characterised. Therefore, such information was retrieved from experimental outcomes reported in the literature for the same material and manufacturing technology [7]. Those estimates were explicitly employed during the establishment of the defect-based fatigue model – it will be shown later how EH model required this information. Nevertheless, analogous to the fatigue endurance limit, an explicit report of the employed values was not possible due to confidentiality matters. A normalised quantity referring to the fatigue SIF threshold is defined as follows:

$$\kappa_{th} = \frac{\Delta K_{th,lc,EBM}}{\Delta\sigma_{w,EBM}\sqrt{\sqrt{\text{area}_0}_{EBM}}} \tag{12}$$

It is important to stress that the purpose of the paper is not to report precise estimates of fatigue performance and defect characteristics of the tested material, but rather to propose a defect-based fatigue modelling reference curve capable of generalising the behaviour of this class of material in the presence of different types of flaws.

## 3. Statistical characterisation of defects: Data analysis and results

### 3.1. Bulk defects

Statistical description of bulk defects can be achieved through both fractography analyses over a significant number of fatigued samples, or via CT analysis of a limited number of samples.

In the present work, both techniques were employed. Regarding the CT analyses, details of the experimental setup and processing parameters utilised for the CT scans are the same as those reported in the authors' previous publications [35]. Without dwelling on the details of the CT analysis, it is important to recall that the highest realistically achievable lateral resolution was 12 μm, therefore, defects showing dimensions smaller than at least twice this value are hardly detectable in a reliable way. For this reason, the identification of defects in materials produced through the SLM technology was scarcely discernible in the present work, due to their relatively small dimensions, especially when compared with those found in EBMed materials. In fact, precise CT identification and following quantification of bulk defects on the EBM batches was successfully achieved. It is important to highlight that a detailed calibration of the defect identification procedure using this technique was exploited; relevant details are reported in the same previous publication of the authors [35].

The sampling strategy block maxima, described in **Section 2.2**, was used to estimate the extreme statistics distribution of the maximum defect size (i.e., $\sqrt{\text{area}}$) inside the gauge volume of the Ti-6Al-4V alloy produced by EBM. The sizes of the defects identified by CT scanning of the specimens were considered in the following procedure. Specifically, the values $\sqrt{\text{area}}$ were obtained with a digital grey threshold (DGT) value equal to 110% set in the VGEasyPore® CT reconstruction routine.

The CT analyses reconstructed the defects present within a volume slightly extended in length from the whole cylindrical gauge part of the

**Table 2**
CT post-processing details for definition of EVS analysis.

| Parameter | Value |
|---|---|
| Number of sub-volumes for each specimen | 8 |
| Volume of each sub-volume $V_0$ | 53.46 mm$^3$ |
| Total inspected volume of each specimen $V_{tot}$ | 427.65 mm$^3$ |
| Volume of the gauge part of each specimen $V_g$ | 392.01 mm$^3$ |
| Total number of sub-volumes (n. specimens × n. sub-volumes) | 40 |

dog-bone sample; this procedure is repeated five times for five different samples. Probed volumes $V_{tot}$ are considered (see Fig. 2**(a)** for the sizes, the volume is a cylinder with a diameter equal to 5.5 mm and 18 mm in length). It is important that the volume considered in this step is kept almost the same for each specimen. After the defect reconstruction of the whole probed volume, such a volume is subdivided into smaller volumes of an equal size, $V_0$. In particular, 8 sub-volumes for each specimen are taken into account (see Fig. 2**(b)**). Details about the specific values used for these analysis steps are provided in Table 2. The volume of the gauge part of the specimen, $V_g$, is also listed, as it is useful to find the Gumbel distribution for the volume of the specimen subjected to the maximum stress through the return period. Following, as detailed in the previous paragraph, the maximum defect size for each sub-volume is selected, and all the values are sorted in ascending order to compute the empirical cumulative distribution function of Eq. (4). Finally, the scale and location parameters were estimated using Eq.(5) and (6).

These steps were performed considering all the specimens of one batch together (i.e. the as-built (N) and machined (NT) batches were processed separately). Confidence bands at each percentile were also drawn using Eq. (9).

Here, it is important to make some remarks about the number of sub-volumes and the size of the control volume. In fact, increasing the number of sub-volumes for each specimen reduces the control volume $V_0$ and, hence, reduces the confidence in the predicted maximum defect size on a larger volume $V_c$. Furthermore, an excessively small control volume could not satisfy the asymptotic distribution of the maxima (i.e. the local maxima are the maxima of a too small number of defects that are not representative of the real distribution). On the contrary, a small number of sub-volumes increases the uncertainty of the estimates of the Gumbel distribution. For these reasons, a trade-off between the number of sub-volumes and the control volume size should be sought to satisfy a reasonable confidence level in the estimate of the prospective maximum defect size.

### 3.1.1. *Results*

As far as the EBM batches are concerned, the outcome of the EVS evaluation done through the CT and fractography analyses are displayed in Fig. 3. The defect size $\sqrt{area}$ for bulk defects was transformed to an

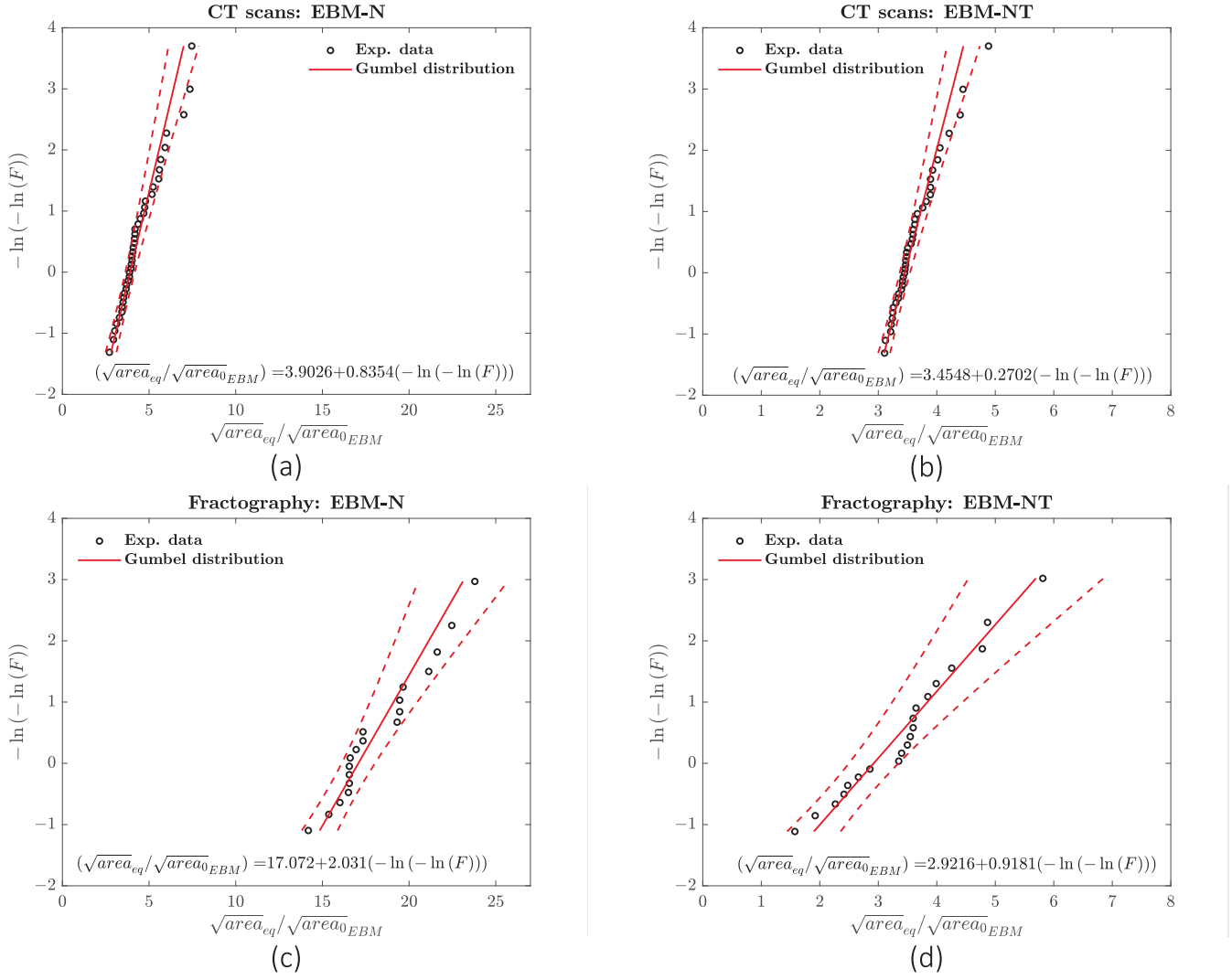


**Fig. 3.** Evaluated Gumbel's distributions of normalised maximum defect size ($\sqrt{area}$) for different EBMed materials under different conditions. (a) CT evaluated for EBM-N, (b) CT evaluated for EBM-NT, (c) Post-mortem fractographic evaluated for EBM-N, (d) Post-mortem fractographic evaluated for EBM-NT.

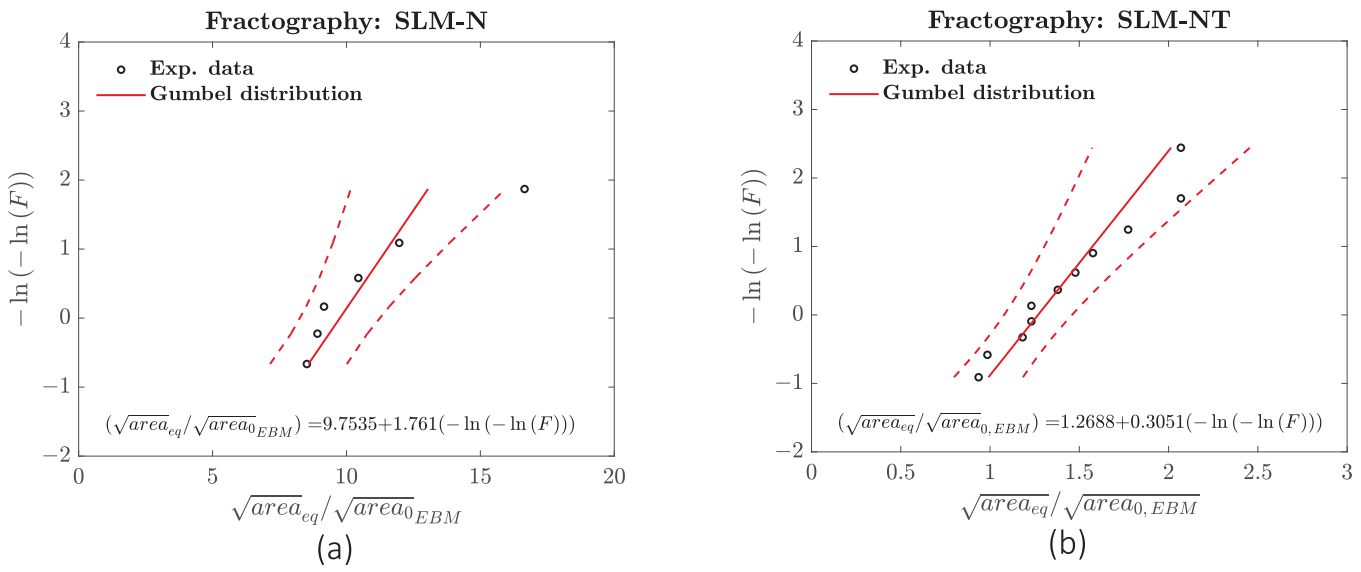


**Fig. 4.** Evaluated Gumbel's distributions of normalised maximum defect size ($\sqrt{\text{area}}$) for (a) SLM-N and (b) SLM-NT materials, evaluated through post-mortem fractographic analysis.

**Table 3**
Estimated location and scale parameters (normalised) of the Gumbel distribution EBMed samples obtained through CT and fractographic analyses regarding as-built (EBD-N) and machined specimens (EBM-NT).

| Batch | Analysis type | $\hat{\mu}_{ML}$ | $\hat{\sigma}_{ML}$ |
|---|---|---|---|
| EBM As-built (EBM-N) | CT | 3.9026 | 0.8354 |
| | Fractography | 17.072 | 2.0310 |
| EBM Machined (EBM-NT) | CT | 3.4548 | 0.2702 |
| | Fractography | 2.9216 | 0.9181 |
| SLM As-built (SLM-N) | Fractography | 9.7535 | 1.7610 |
| SLM Machined (SLM-NT) | Fractography | 1.2688 | 0.3051 |

equivalent defect size, $\sqrt{\text{area}}_{eq}$, by adopting a reference crack shape factor equal to 0.65, i.e. for sub-surface defects. This operation assumes the conservation of the SIF intensity associated with the considered defect ($\Delta K = \Delta K_{eq}$), as explained in **Section 4**.

A few remarks can be drawn regarding the results shown in Fig. 3. First of all, there exists a good match between the distributions of extreme defects for the EBM-N and EBM-NT samples. This is plausible because, regardless of the surface finish, the CT analysis only accounted for bulk defects due to its methodological nature. It is interesting to note that for the samples subjected to surface machining (EBM-NT), although the normalised location $\hat{\mu}_{ML}$ appears to be comparable, the normalised scale parameter $\hat{\sigma}_{ML}$ turned out to be rather different. This may be due to the different statistical significance of the two datasets.

As far as the as-built material conditions are concerned (EBM-N), only fractography can capture the defects that trigger fatigue cracks, i.e., surface killer defects, whereas CT analysis cannot accurately detect the surface features that initiate cracks.

As said earlier, regarding the SLM samples, the limited number of detectable defects hampered their CT detection. Therefore, only the EVS distribution obtained via the fractography analysis could be conducted. The result is shown in Fig. 4 for both the as-built and machined batches.

As a summary, Table 3 reports all the estimates of the Gumbel distributions obtained in the present work. The location parameter $\hat{\mu}_{ML}$ estimated from killer defects in fractographic analysis is slightly smaller for the SLM-NT batch than the EBM-NT, further confirming that using the HIP treatment is more beneficial for the EBM material. It is important to note that the HIP post-process effectively closed bulk defects, making them undetectable via CT. Similarly, fractographic observations showed no striking evidence of defects driving fatigue crack nucleation.

**Table 4**
Surface roughness scanning parameters for estimating the EVS distribution.

| Parameter | Value |
|---|---|
| Number of investigated specimens | 5 |
| Reference area size,$A_0$ | $0.8 \times 0.8 = 0.64$ mm$^2$ |
| Total number of investigated areas | 8 $A_0$/specimen with 40 $A_0$ in total |
| Surface area of the gauge length,$A_g$ | $16.5 \times \pi \times 5.5 = 285.09$ mm$^2$ |
| Return period $A_g/A_0$ | 445.47 |

Instead, high-magnification SEM analysis revealed that nucleation was triggered by other, smaller microstructural features rather than traditional pores. Consequently, EVS characterisation excluded the HIP-treated samples to avoid a highly unreliable assessment. Nevertheless, the dimensions of these microstructural features were measured to locate the fatigue data points for the EH curve determination. It is also significant that while the $\sqrt{\text{area}}$ measurements of these features may contain errors, they have a negligible impact on the overall position of the points on the EH curves. As mentioned above, the large discrepancy in the Gumbel distribution parameters estimated from fractography and CT for the EBM-N (as-built) specimens is due to the different nature of the defects detected by the two methods. In other words, the CT probed only the statistical distribution of bulk defects, whereas the fractography can detect the surface defects at the origin of the failure.

### 3.2. Surface defects (roughness)

As far as the surface roughness characterisation of the material before fatigue testing is concerned, again for predictive purposes, optical microscopy was utilised over several samples for each AM technology. In this section, the same n.5 samples that were inspected by CT, are considered to show the extreme value distributions related to surface defects in EBM and SLM. The employed probing instrument was able to achieve a resolution as high as 7 μm. Table 4 presents additional post-processing parameters used for the evaluation of the EVS distribution. It is important to note that this section utilises only 5 specimens for the purpose of comparison with the trends observed in the EVS distribution, as well as the trends previously reported in the CT evaluation of the EVS. However, the areal study of the $S_v$ for each fatigue-tested sample was carried out to entirely populate the Kitagawa diagram displayed in Fig. 6 and Fig. 7, which enabled the EH curve identification.

The extreme value distribution of the maximum equivalent defect

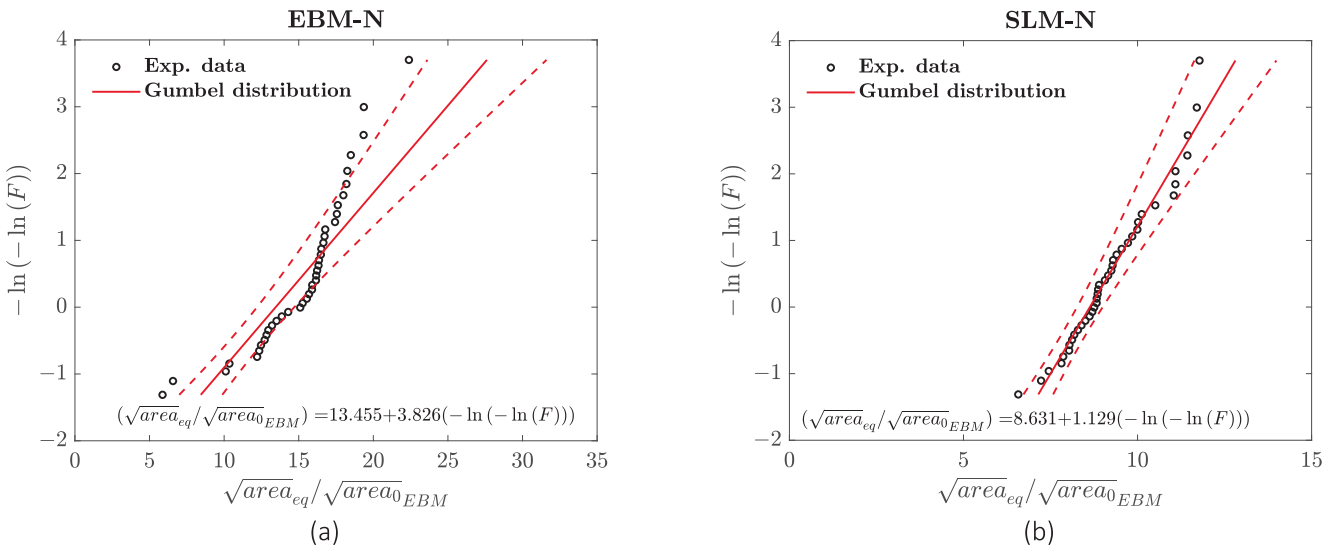


**Fig. 5.** Estimated Gumbel distributions of maximum pit depth parameter, considering an equivalent projected area ($\sqrt{\text{area}}_{\text{eq}}$). (a) as-built EBM batch (N); (b) as-built SLM batch (N).

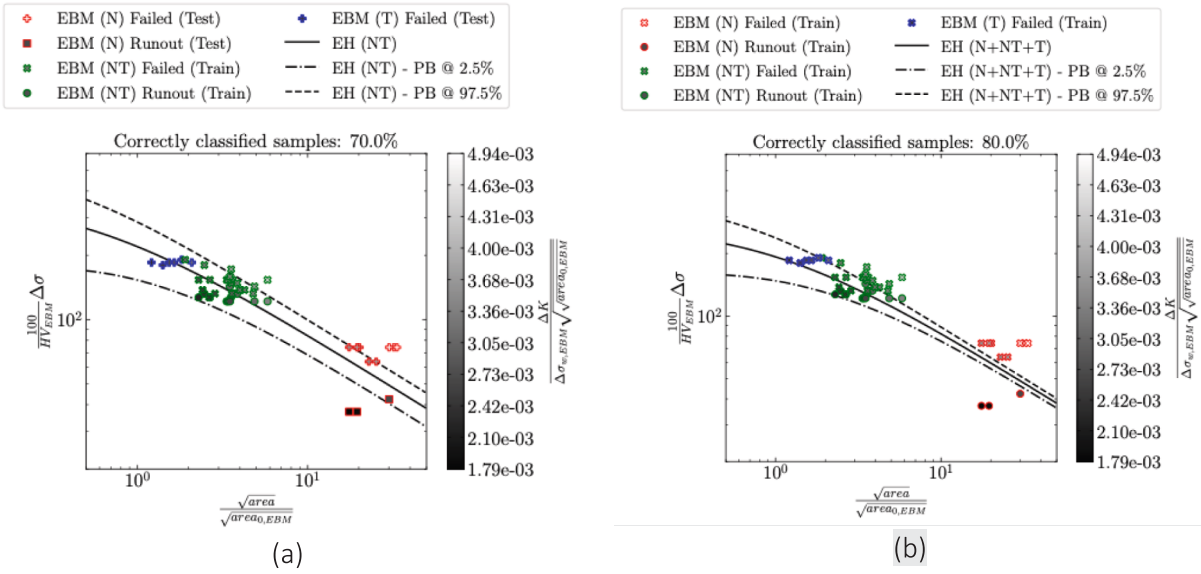


**Fig. 6.** Identified fatigue curves for the EBM batch. (a) identification conducted by exploiting only turned (NT) samples and $\Delta K_{th,lc}$. (b) identification conducted by exploiting all the available fatigued samples. In both cases the prior over $\Delta K_{th,lc}$ is determined upon the conducted fatigue crack growth test. Each panel also report, as a percentage, the correctly classified sample over the total number of samples. In the legend, PB stands for Prediction Band.

size, $\sqrt{\text{area}}_{\text{eq}}$, can be obtained using the same procedure adopted for the maximum defect size distribution from CT (**Section 3.1**).

The maximum pit depth parameter was acquired for 8 sub-areas with a size equal to $A_0$ for each selected specimen. The number of sub-areas was deliberately set equal to the number of sub-volumes used in CT data analysis. To avoid analysing a large, rounded surface of the specimen, which requires rotating the samples during scanning and then unrolling during post-processing, the sub-area size was set to $0.8 \times 0.8$ mm$^2$. This choice allows scanning the surface along the gauge length without rotating the sample. This methodology is equivalent to a block maxima sampling strategy; therefore, once the values of the maximum pit depth parameter are obtained from the surface roughness acquisitions, they can be converted to the equivalent $\sqrt{\text{area}}_{\text{eq}}$ using Eq. (15). Then, the parameters of the Gumbel distribution are estimated as described in Section 2.2. It must be noted that the maximum values of $S_v$ are referred to a control area $A_0$, instead of a control volume $V_0$, and, thus, the Gumbel distribution is referred to the maximum values of $S_v$ in an area equal to $A_0$. Similar to $V_g$, Table 4 reports also the surface area of the gauge part, $A_g$, necessary to evaluate the return period for one specimen.

The Gumbel distribution was estimated for each specimen but was also obtained considering all the specimens of one batch together. Confidence bands at each percentile were also drawn.

### 3.2.1. Results

The outcome of the EVS evaluation is shown in the two plots depicted in Fig. 5. The comparison between single specimens is reported in Appendix A. for completeness.

It is apparent that the EBM technology returns a surface morphology that differs from the SLM counterpart. The normalised location $\hat{\mu}_{\text{ML}}$ and the normalised scale parameter $\hat{\sigma}_{\text{ML}}$, are slightly higher for the EBM samples. This is translated into a more detrimental impact on the fatigue performance, assuming equal fatigue intrinsic property of the two ma-

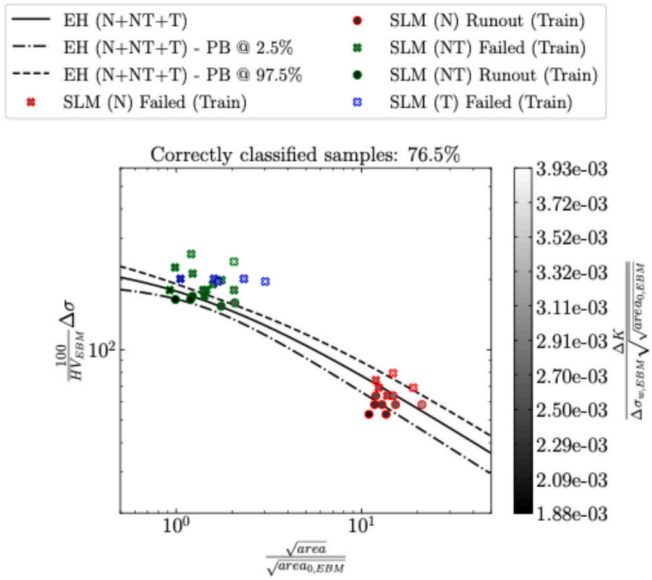


**Fig. 7.** Identified fatigue curves for the SLM batch. Identification conducted by exploiting only turned (NT) samples and $\Delta K_{th,lc}$ surveyed from the literature. This figure also reports, as a percentage, the correctly classified sample over the total number of samples. In the legend, PB stands for Prediction Band.

**Table 5**
Estimated location and scale parameters (normalised) of the Gumbel distribution of maximum pit depth parameter for as-built EBM (N) and SLM (G) batches using equivalent projected area ($\sqrt{area}_{eq}$).

| Batch | $\widehat{\mu}_{ML}$ | $\widehat{\sigma}_{ML}$ |
|---|---|---|
| EBM – As-built (N) | 13.46 | 3.826 |
| SLM – As-built (N) | 8.631 | 1.129 |

terials (that it is not true).

Finally, a summary of the retrieved values for the EVS evaluation is shown in Table 5.

## 4. Fatigue model identification and results

As already mentioned in Section 2.3, the EH model describes the relationship between the fatigue endurance limit at a prescribed number of cycles $N^*$ and the defect size in the so-called Kitagawa diagram. This diagram depends on the material, post-processing conditions, stress ratio R and crack shape factor Y.

In the present work, the Kitagawa diagram is drawn for $R = 0.1$, since all fatigue data are collected at this stress ratio. Only when fatigue data are collected at different stress ratios, a mean stress correction is necessary.

Similarly to the stress ratio, fatigue data that exhibit failures from different types of defects, e.g. bulk and sub-surface defects, can be plotted in the same diagram by considering a reference crack shape factor and hypothesising the same SIF value. The rationale behind this hypothesis is that we can define an equivalent defect size by adopting the same crack shape factor for all defect types but maintaining the same defect harmfulness, i.e. the same SIF value. In this work, the reference crack shape factor is equal to 0.65, i.e. the Kitagawa diagram is plotted for sub-surface defects. Hence, for each bulk defect ($Y = 0.5$), the equivalent defect size ($\sqrt{\text{area}}_{\text{eq}}$) is calculated from the SIF equality ($\Delta K = \Delta K_{eq}$):

$$\Delta\sigma\, 0.5\sqrt{\pi\sqrt{\text{area}}} = \Delta\sigma 0.65\sqrt{\pi\sqrt{\text{area}}_{\text{eq}}} \tag{13}$$

which leads to the following equation:

$$\sqrt{\text{area}}_{\text{eq}} = \left(\frac{0.5}{0.65}\right)^2\sqrt{\text{area}} \tag{14}$$

Therefore, the equivalent defect size of bulk defects is lowered by a factor of $(0.5/0.65)^2$ to guarantee a constant SIF value associated with the considered defect.

Specimens in as-built conditions always failed at the surface due to asperities in the roughness profile, contrary to machined specimens. In that case, the maximum pit depth parameter, $S_v$, has been proven to be well-correlated with the fatigue limit of additively manufactured metal in as-built conditions [7]. To adopt this parameter in a fracture mechanics approach, the value of $S_v$ must be inserted into the SIF formula. At this stage, different hypotheses can be assessed to associate the effect of the maximum pit depth parameter to a crack configuration and, therefore, to a specific SIF formula. Clearly, all the crack configurations considered must be referred to as surface cracks. If the Murakami parameter, $\sqrt{\text{area}}$, is used, the shape factor Y is equal to 0.65, whereas an equivalent $\sqrt{\text{area}}$ must be derived from the value of $S_v$.

In our specific case, the crack configuration that best correlates with the experimental fatigue limit is the shallow surface defect [4,7], where the equivalent $\sqrt{\text{area}}$ is calculated as follows ($Y = 0.65$):

$$\sqrt{\text{area}}_{\text{eq}} = \sqrt{10}\,S_v \tag{15}$$

Other crack configurations that were evaluated yielded equivalent defect sizes smaller than the shallow crack above, underestimating the fatigue limit and providing a too small SIF threshold for long cracks compared to the literature.

### 4.1. Identification framework for El Haddad curves

As mentioned in Section 2.3, B-FADE algorithm was employed to conduct the probabilistic identification of the EH curve under the two considered manufacturing conditions, i.e. EBM and SLM. Although the complete framework of B-FADE can be found elsewhere [45], it is worth recalling its main stages.

In essence, B-FADE turns the EH curve into the decision boundary of the collected dataset:

$$D = \{((\Delta K_i, \Delta\sigma_i, Y_i), F_i)\,|\,i = 1, 2, \cdots, M; F_i = \{0, 1\}\} \tag{16}$$

which collates information about fatigue testing and characteristic defect sizes responsible for failure, and $F_i$ takes either 0 or 1 if the ith sample run-out or failed, respectively. B-FADE transforms the phenomenological behaviour of the EH curve into a classification problem. Upon setting $\theta = [\Delta K_{th,lc} \quad \Delta\sigma_w]$ as the aggregated vector of the unknown EH parameters, a full probability distribution over $\theta$ is found through Maximum a Posteriori (MAP) estimation, which relies on Bayes' theorem:

$$P[\theta|D] = \frac{P[D|\theta]\,P[\theta]}{P[D]} \tag{17}$$

$P[\theta|D]$ Posterior distribution
$P[D|\theta]$ ~ Bernoulli likelihood of D.
$P[\theta]$ Prior distribution
$P[D]$ evidence.

It is worth emphasising that the prior (distribution) $P[\theta]$ in Eq. (17) is the knowledge of the modeller about the parameters, before observing any data in D. Specifically, the prior distribution confers the user the freedom of injecting pertinent information about the parameters, whether from the literature or previous experiments. In the present work, the authors assumed the following joint prior distribution for $\theta$:

$$P[\theta] = P\left[\Delta K_{th,lc}\right]P[\Delta\sigma_w] \tag{18}$$

**Table 6**
Model identification criteria and employed datasets.

| | EBM | SLM |
|---|---|---|
| **Training datasets** | i) EBM-NT; ii) EBM-N + EBM-NT + EBM-T | iii) SLM-N + SLM-NT + SLM-T |
| $\Delta\sigma_w$ | Uniform prior | Uniform prior |
| $\Delta K_{th,lc}$ | i), ii) Gaussian prior experimentally evaluated | Gaussian prior distribution from the literature |

which implies initial independence between the parameters. As far as the present material datasets are concerned, it is worth emphasising that no prior information was leveraged for $\Delta\sigma_w$ under both manufacturing conditions EBM and SLM. Therefore, a uniform prior $P[\Delta\sigma_w] \sim U$ were prescribed over this parameter, thus giving priority to the experimental evidence. Conversely, $P\left[\Delta K_{th,lc}\right]$ was shaped by experimental fatigue crack growth and literature data for the EBM and SLM batch, respectively.

Specifically, let $\Delta K_{th,lc}{}^{(i)}$ be the i-th of L values the SIF threshold either retrieved from the experiment or recovered from literature. Accordingly, the normalised mean is computed as follows:

$$m = \frac{1}{L}\sum_{i=1}^{L} \kappa_{th}{}^{(i)} \tag{19}$$

and the unbiased estimator of the standard deviation (not normalised) is:

$$s = \sqrt{\frac{1}{L-1}\sum_{i=1}^{L}\left(\mu - \Delta K_{th}{}^{(i)}\right)^2} \tag{20}$$

As for the EBM batch, n.3 tests were conducted, hence $L = 3$, whereas for SLM samples $L = 13$ values were found from the literature [7,46]. Given μ and σ, the corresponding Gaussian distribution is readily defined. The normalised numerical values of the distributions' parameters are given later in the forthcoming sections.

Following MAP, the posterior underwent Laplace's approximation, so $P[\theta|D]$ is approximated with a bivariate Gaussian distribution. Its statistical post-processing enables one to compute the prediction interval of the associated EH curve.

### 4.2. Generalised El Haddad model identification

This section illustrates the results of the identification of the EH curve for the EBM and SLM batches of samples. Firstly, the defects responsible for the fatigue failure must be identified and assigned with an equivalent size previously defined as $\sqrt{\text{area}}_{eq}$, see Eq.(14), depending on their nature, i.e., bulk ($Y = 0.5$) or surface ($Y = 0.65$). This allows one to represent all the examined sample over a unique Kitagawa diagram. As far as the sample that underwent machining (i.e., EBM-NT, EBM-T, SLM-NT and SLM-T) are concerned, the analysis of the fracture surface enabled the unambiguous identification of the killer defect, therefore this approach was pursued. Conversely, fractographic analysis of the as-built samples, such as EBM-N and SLM-N, did not lead to a direct identification and quantification of the feature that determined the fatigue failure origin. For this reason, the associated $\sqrt{\text{area}}_{eq}$, see Eq. (15), for each failed as-built sample was assessed by exploiting the EVS retrieved before mechanically testing the samples. It is worth mentioning that a limited areal scan of each sample was carried out for the definition of the EVS and the extrapolation to account for the actual surface extent of each sample was attained by using the return period, see **Eq. (7)**. Further information regarding the EVS of the two as-built batches are provided in **Section 3.2**. The employed approaches for the equivalent defect size identification, $\sqrt{\text{area}}_{eq}$, of different batches are summarised as follows:

- Killer defect $\sqrt{\text{area}}$ from fractography: EBM-NT, EBM-T, SLM-NT, SLM-T
- Maximum $S_v$ from areal scan of the sample surface: EBM-N, SLM-N

For the sake of clarity is worth giving a synopsis of the hypothesis considered for the present training stage, as displayed by Table 6.

Regarding the EBM samples, a preliminary identification was carried out for the purpose of validating the proposed unified approach. In particular, the EH curve and associated prediction intervals were first evaluated by only considering fatigued samples which underwent machining (EBM-NT), and by considering a prior knowledge of the fatigue SIF threshold provided by the experiments as a Gaussian prior distribution, case (i). Dimensions of killer defects (i.e., $\sqrt{\text{area}}$) were evaluated through fractographic post-mortem analysis. For runout samples, the link to a characteristic defect size was established by testing the samples a second time over a much higher stress range until failure – this process enabled locating two points on Kitagawa's diagram, one for a runout sample and one for a failed sample sharing the same $\sqrt{\text{area}}$ value. It is reasonable that fatigue loading over a small stress range, leading to runout, introduces a small amount of damage, though it is difficult to quantify. Nevertheless, this small fatigue damage can be neglected if the following test on the same specimen is performed at a significantly higher stress range, making the procedure of retesting runout samples acceptable.

A subsequent superposition of the remaining datasets (i.e., EBM-N and EBM-T) over the previously evaluated fatigue curve allowed for the confirmation of the validity of the proposed approach, see Fig. 6**(a)**. Indeed, experimental points referring to EBM-N and EBM-T batches are correctly separated by the EH curve and the intrinsic scatter is well captured by the prediction band. It is worth recalling from **Section 2.2** that the characteristic defect size of as-built samples (EBM-N) in Kitagawa's diagram refers to the maximum expected $\sqrt{\text{area}}_{eq}$ associated with the EVS distribution of $S_v$, not to the killer defects. To obtain the maximum expected value, the return period was adopted to scale up the EVS distribution to the surface area of the gauge length from the reference area size where local maxima of $S_v$ were collected.

Given that the adoption of a single EH curve can accurately capture a multitude of material conditions, this proves defects to be the key factor dominating the fatigue performance of this material. It is important to remark that the HIP treatment has an effect on the microstructure of the base material, which in turn it affects its intrinsic fatigue properties. Nevertheless, by considering the hardness as a parameter that correlates well with the fatigue performance of a material, it is important to state that the hardness of the T material condition differs only slightly from that of the N and NT samples. This value can be considered negligible and thus it is sound to use a unified curve to characterise the fatigue response of the investigated material.

Having said that, it is therefore reasonable to improve the identification of the EH model by including all the available fatigue points (i.e., N, NT and T), considering again the experimentally estimated $\Delta K_{th,lc}$. The outcome of the final identification process is shown in Fig. 6**(b)**. It is apparent that the estimated EH curve better separates the runout points from those depicting failed samples. The percentages of the correctly classified samples, reported in both Fig. 6 **(a)** and **(b)**, confirm that, by considering all batches together, the accuracy improves from 70% to 80%. Moreover, prediction bands are now considerably narrower than the previous identification. In particular, the leftmost side of the band is narrower because of the accounting of the points referring to the as-built conditions, which confirm the validity of $\Delta K_{th,lc}$ prior knowledge obtained from experiments. As an outcome, the uncertainty of the EH curve near the $\Delta K_{th,lc}$ region is further reduced.

The EBM-T batch occupies the region of the Kitagawa diagram for very small defect sizes, whereas the EBM-NT generally exhibits slightly larger defect sizes. Therefore, the two batches together cover a wide range of defect sizes. Interestingly, although the EBM-N occupies a

**Table 7**
Marginal prior & posterior distribution of the EH parameters for the EBM batch (batch classification according to Table 6).

| | Non-dimensional $\Delta K_{th,lc}$ distributions | Non-dimensional $\Delta\sigma_w$ distributions |
|---|---|---|
| **Prior** | $P\left[\frac{\Delta K_{th,lc,EBM}}{\Delta\sigma_w\sqrt{\sqrt{area_0}_{EBM}}}\right] \sim N(3.13\text{x}10^{-3}, 0.125^2)$ | $P\left[\frac{\Delta\sigma_w 100}{HV_{EBM}}\right] \sim \text{U}$ |
| **Posterior Batch (i)** | $P\left[\frac{\Delta K_{th,lc,EBM}}{\Delta\sigma_w\sqrt{\sqrt{area_0}_{EBM}}}\right] \sim N(3.14\text{x}10^{-3}, 0.12^2)$ | $P\left[\frac{\Delta\sigma_w 100}{HV_{EBM}}\right] \sim N(370, 465^2)$ |
| **Posterior Batch (ii)** | $P\left[\frac{\Delta K_{th,lc,EBM}}{\Delta\sigma_w\sqrt{\sqrt{area_0}_{EBM}}}\right] \sim N(3.14\text{x}10^{-3}, 0.13^2)$ | $P\left[\frac{\Delta\sigma_w 100}{HV_{EBM}}\right] \sim N(272, 242^2)$ |

**Table 8**
Marginal prior and posterior distribution of the EH parameters for the SLM batch (batch classification according to Table 6).

| | Non-dimensional $\Delta K_{th,lc}$ distributions | Non-dimensional $\Delta\sigma_w$ distributions |
|---|---|---|
| **Prior** | $P\left[\frac{\Delta K_{th,lc,SLM}}{\Delta\sigma_w\sqrt{\sqrt{area_0}_{EBM}}}\right] \sim N(2.79\text{x}10^{-3}, 2.05^2)$ | $P\left[\frac{\Delta\sigma_w 100}{HV_{EBM}}\right] \sim \text{U}$ |
| **Posterior** | $P\left[\frac{\Delta K_{th,lc,SLM}}{\Delta\sigma_w\sqrt{\sqrt{area_0}_{EBM}}}\right] \sim N(2.97\text{x}10^{-3}, 0.54^2)$ | $P\left[\frac{\Delta\sigma_w 100}{HV_{EBM}}\right] \sim N(246, 123^2)$ |

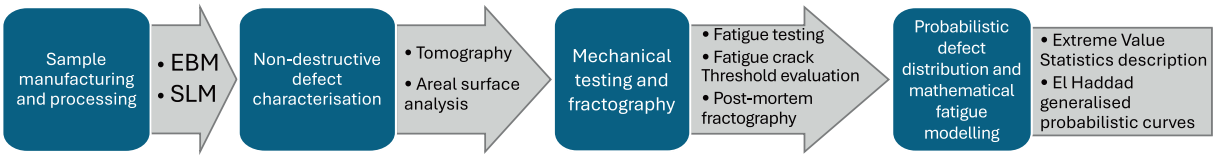


**Fig. 8.** Flowchart of the material characterisation and modelling of the generalised defect-based fatigue framework.

region of the Kitagawa diagram far from the other batches, the estimated EH curve can confidently predict the fatigue limit between the EBM-NT and EBM-N characteristic defect sizes, as seen in the small width of the prediction band. The same is not true for the part of the EH curve close to the defect-free fatigue endurance limit, where the prediction band widens.

The final identification shown in Fig. 6**(b)** led to the definition of an EH curve having the distributions of its driving parameters labelled as "Posterior" in Table 7. For the sake of completeness, the prior knowledge employed for the identification is also displayed in the table, labelled as "Prior".

Regarding the SLM specimens, as said earlier, the experimental $\Delta K_{th,lc}$ was not available, therefore, the issue related to the lack of information must be coped with by hunting data from the pertinent literature [7,46]. The training of the EH model was conducted by considering all the SLM batches available. The plot shown in Fig. 7 portrays the final results of the analysis, i.e. the estimated EH curve and the associated prediction intervals. Again, the model can precisely discriminate the runouts and failed points belonging to the as-built conditions (N), providing a reliable EH curve. Unlike the EBM batch, the rightmost part of the prediction band widens given the relatively higher spread of the prior distribution and lower density of training samples. Despite the lack of experimental information regarding $\Delta K_{th,lc}$, the prior information shaped from the literature suffices to inject adequate training information to accomplish MAP. Whilst the data points correctly guide the EH curve throughout the training, as substantiated by the considerably narrower prediction interval in the rightmost portion of the figure. Overall, the estimated EH curve well tracks the conformation of the dataset with 76.5% correct classified samples, and the prediction interval captures the scatter of the data. It can be, therefore, concluded that the estimated curve appropriately characterises the fatigue endurance limit for the SLM samples in all manufacturing conditions, and it can be exploited for the design against fatigue failure. As a final remark, the SLM-NT and SLM-T specimens populate the same region of Kitagawa's diagram, showing that the machined and hipped SLM specimens have similar killer defect sizes or microstructural features at the origin of the crack nucleation.

Quantitative information about the injected prior knowledge and the following estimated EH parameters is summarised in Table 8.

Eventually, the actions required to fully implement the generalised framework are schematically displayed in Fig. 8. To help future researchers and structural engineers exploit the proposed approach.

## 5. Conclusions

This research successfully established a unified probabilistic framework for estimating the fatigue endurance limit of Ti-6Al-4V alloy produced via Selective Laser Melting (SLM) and Electron Beam Melting (EBM). By integrating experimental data with prior material knowledge, the approach generated two distinct fatigue endurance limit curves that account for the synergistic effects of bulk and surface defects. A key innovation of this method was treating the $S_v$ surface roughness parameter as an equivalent crack $\sqrt{area_{eq}}$, and utilising Murakami's $\sqrt{area}$ parameter for internal defects, while making these two defect characteristic dimensions physically comparable when determining the fatigue curves. The integration of literature data proved vital, particularly for SLM conditions where experimental stress intensity factor thresholds were unavailable. Through the application of Extreme Value Statistics (EVS) to both Computed Tomography (CT) and fractographic data, the study demonstrated that Hot Isostatic Pressing (HIP) effectively eliminated bulk defects. Consequently, the fatigue strength of HIP-treated batches was found to be governed solely by the material's intrinsic properties rather than manufacturing flaws. Despite these successes, the modelling of surface roughness remains the primary source of uncertainty. Future work should focus on:

- Correlating fractographic evidence more closely with surface topography for "killer" defects.
- Extending the model to predict finite fatigue life.

- Validating the transferability of EVS characteristics from simple laboratory specimens to complex, net-shape components.

In conclusion, the proposed model offers a robust tool for the probabilistic evaluation of fatigue limits and holds significant promise for the design of notched components within numerical structural frameworks.

## CRediT authorship contribution statement

**Enrico Salvati:** Writing – original draft, Visualization, Validation, Supervision, Resources, Project administration, Methodology, Investigation, Funding acquisition, Formal analysis, Conceptualization. **Marco Pelegatti:** Writing – original draft, Visualization, Validation, Methodology, Investigation, Formal analysis, Data curation, Conceptualization. **Marco Petruzzi:** Writing – review & editing, Validation, Software, Methodology, Investigation, Formal analysis, Data curation. **Alessandro Tognan:** Writing – original draft, Visualization, Validation, Software, Methodology, Investigation, Formal analysis, Data curation. **Emanuele Avoledo:** Writing – review & editing, Validation, Software, Methodology, Investigation, Formal analysis, Data curation. **Federico Milan:** Writing – review & editing, Methodology, Investigation, Formal analysis, Data curation. **Francesco De Bona:** Writing – review & editing, Validation. **Niki Picco:** Writing – review & editing, Validation. **Francesco Sordetti:** Writing – review & editing, Validation. **Alex Lanzutti:** Writing – review & editing, Validation, Conceptualization. **Michele Pressacco:** Writing – review & editing, Validation, Resources, Project administration, Funding acquisition. **Riccardo Toninato:** Writing – review & editing, Validation, Resources, Project administration.

## Declaration of competing interest

The authors declare that they have no known competing financial interests or personal relationships that could have appeared to influence the work reported in this paper.

## Acknowledgements

Enrico Salvati would like to acknowledge the European Research Council (ERC) for funding the ERC Starting grant project BREAKDOWN (Grant agreement ID: 101162848). Funds were also received by the project “POR FESR 2021–2027 - Ricerca e sviluppo - Bando 2022 - Progetto EFESTO Prat. N. 2022/76” funded by Regione FVG .

## Appendix A

Gumbel distributions were obtained from surface roughness data for five EBM-N and SLM-N specimens individually, then combined into a joint distribution using data from all specimens in each batch. Fig. 9 and Fig. 10 report the experimental data and the estimated Gumbel distributions for each analysed specimen.

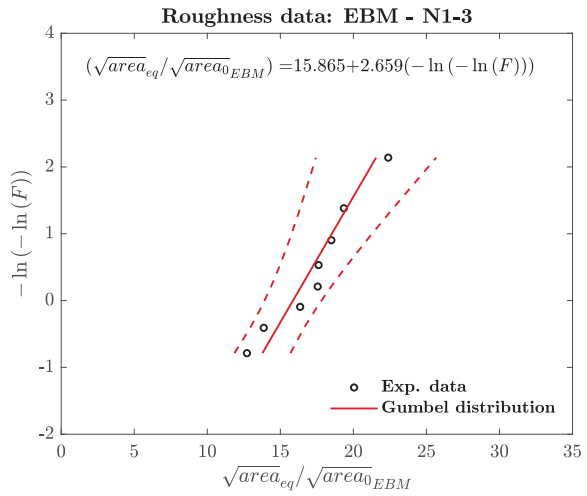


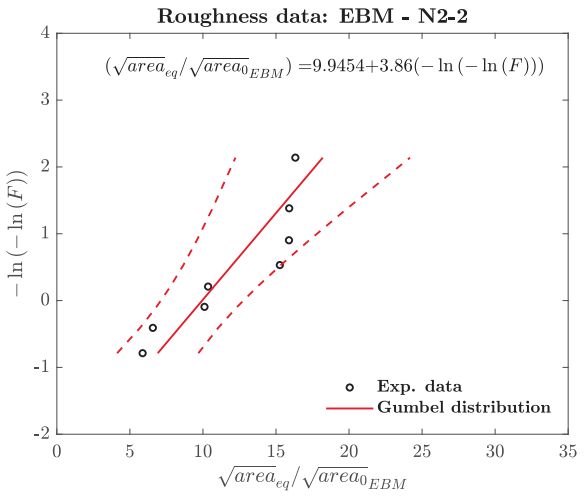


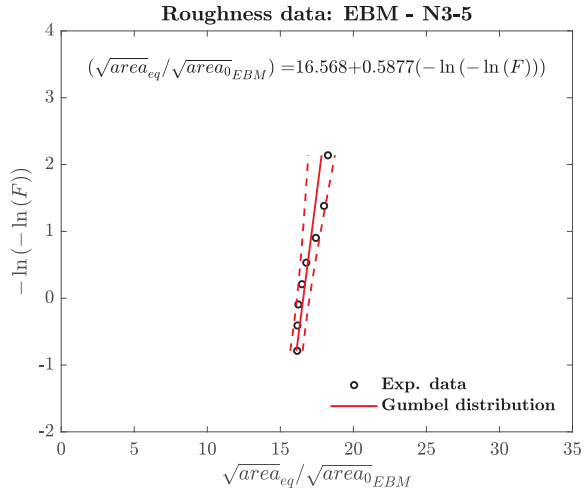


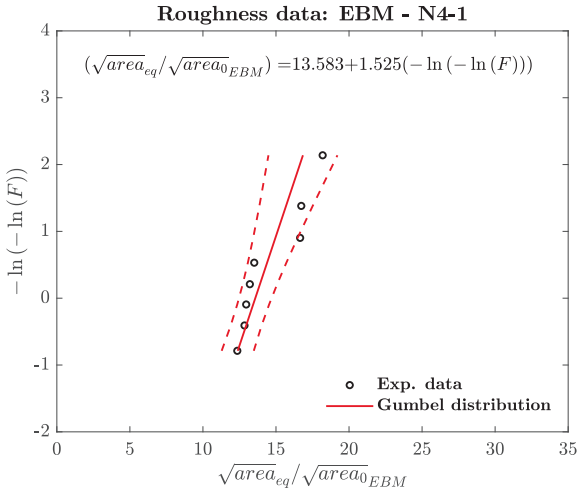


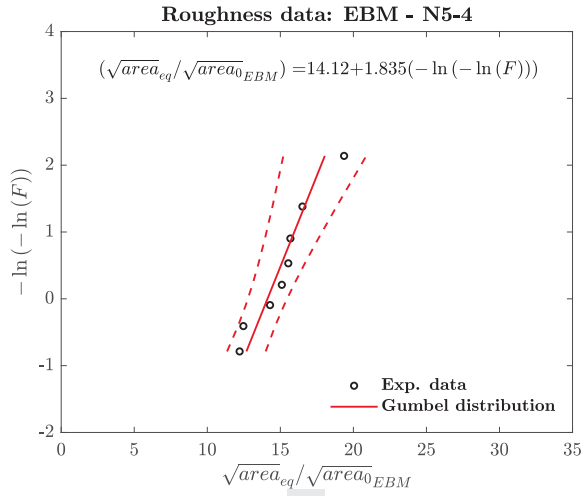


**Fig. 9.** Estimated Gumbel distributions of maximum pit depth parameter, considering an equivalent projected area, for five different EBM-N specimens.

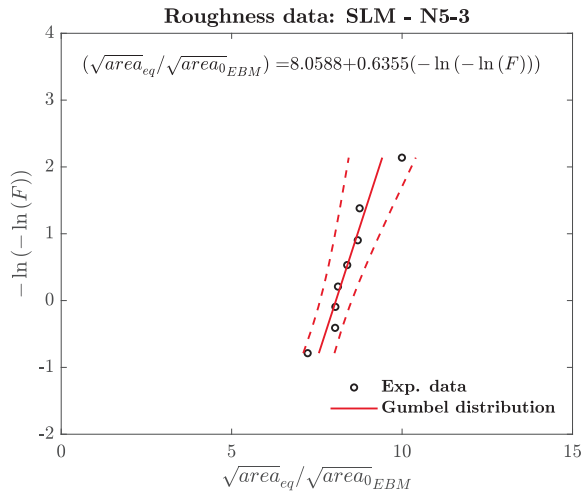


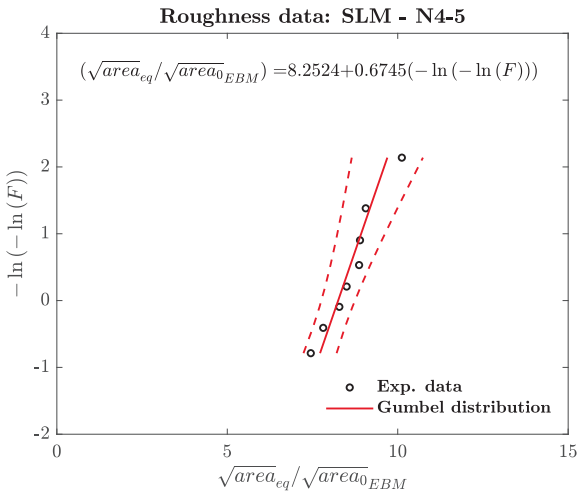


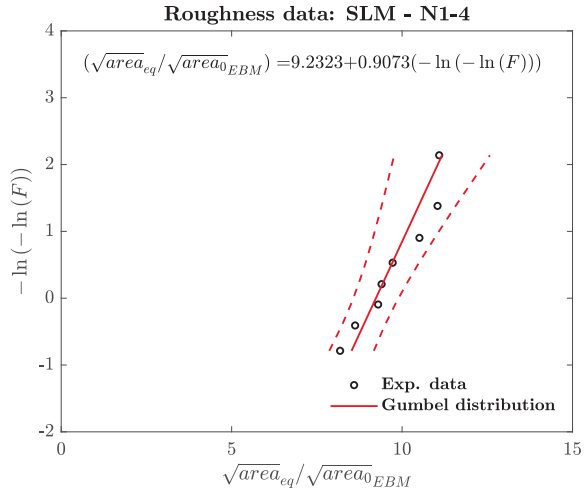


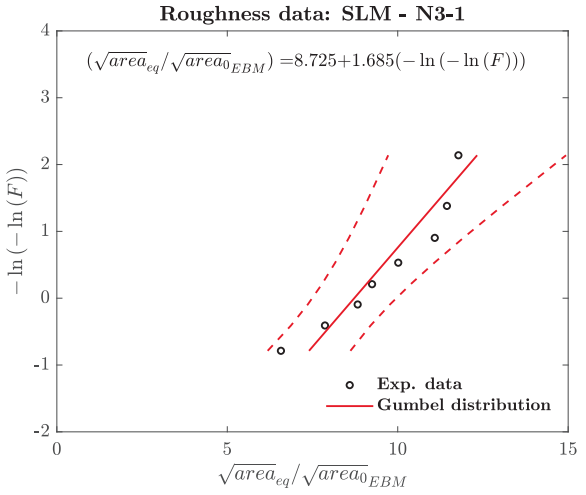


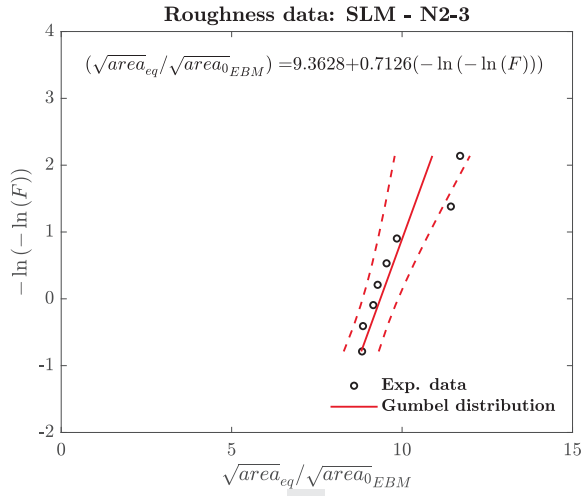


**Fig. 10.** Estimated Gumbel distributions of maximum pit depth parameter, considering an equivalent projected area, for five different SLM-N specimens.

## Data availability

Data will be made available on request.

## References


[1] Frazier WE. Metal Additive Manufacturing: a Review. J Mater Eng Perform 2014;23(6):1917–28.
[2] Brennan M, Keist J, Palmer T. Defects in metal additive manufacturing processes. Springer; 2021.
[3] Sanaei N, Fatemi A. Defects in additive manufactured metals and their effect on fatigue performance: a state-of-the-art review. Prog Mater Sci 2021;117:100724.
[4] Murakami Y. Metal fatigue: Effects of small defects and nonmetallic inclusions. Elsevier; 2019.
[5] Romano S, Brückner-Foit A, Brandão A, Gumpinger J, Ghidini T, Beretta S. Fatigue properties of AlSi10Mg obtained by additive manufacturing: Defect-based modelling and prediction of fatigue strength. Eng Fract Mech 2018;187:165–89.
[6] Yamashita Y, Murakami T, Mihara R, Okada M, Murakami Y. Defect analysis and fatigue design basis for Ni-based superalloy 718 manufactured by selective laser melting. Int J Fatigue 2018;117:485–95.
[7] Rigon D, Coppola F, Meneghetti G. Fracture mechanics-based analysis of the fatigue limit of Ti6Al4V alloy specimens manufactured by SLM in as-built surface conditions by means of areal measurements. Eng Fract Mech 2024;295:109720.
[8] Macoretta G, Romanelli L, Santus C, Romoli L, Lutey AHA, Uriati F, et al. Modelling of the surface morphology and size effects on fatigue strength of L-PBF Inconel 718 by comparing different testing specimens. Int J Fatigue 2024;181:108120.
[9] Romano S, Peradotto E, Beretta S, Ugues D, Barricelli L, Maculotti G, et al. Fatigue strength estimation of net-shape L-PBF Co–Cr–Mo alloy via non-destructive surface measurements. Int J Fatigue 2024;178:108018.
[10] Gillham B, Yankin A, McNamara F, Tomonto C, Taylor D, Lupoi R. Application of the Theory of critical Distances to predict the effect of induced and process inherent defects for SLM Ti-6Al-4V in high cycle fatigue. CIRP Ann 2021;70(1):171–4.
[11] Perghem D, Rusnati L, Patriarca L, Uriati F, Beretta S. Comparison of Fatigue Life and Strength Models for Defective Materials: Application to Scalmalloy in Different Surface Conditions. Fatigue & Fracture of Engineering Materials & Structures 2025;48(7):3185–205.
[12] Dinh TD, Vanwalleghem J, Xiang H, Erdelyi H, Craeghs T, Paepegem WV. A unified approach to model the effect of porosity and high surface roughness on the fatigue properties of additively manufactured Ti6-Al4-V alloys. Addit Manuf 2020;33:101139.
[13] Bao H, Wu S, Wu Z, Kang G, Peng X, Withers PJ. A machine-learning fatigue life prediction approach of additively manufactured metals. Eng Fract Mech 2021;242:107508.
[14] Chen J, Liu Y. Fatigue modeling using neural networks: a comprehensive review. Fatigue & Fracture of Engineering Materials & Structures 2022;45(4):945–79.
[15] Ciampaglia A, Tridello A, Paolino DS, Berto F. Data driven method for predicting the effect of process parameters on the fatigue response of additive manufactured AlSi10Mg parts. Int J Fatigue 2023;170:107500.
[16] Maleki E, Bagherifard S, Unal O, Guagliano M. Hybrid Intelligence approach to study post-processing impact on the mechanical performance of notched additively manufactured AlSi10Mg. Mater Des 2024;248:113462.
[17] Salvati E, Tognan A, Laurenti L, Pelegatti M, De Bona F. A defect-based physics-informed machine learning framework for fatigue finite life prediction in additive manufacturing. Mater Des 2022;222:111089.
[18] Avoledo E, Tognan A, Salvati E. Quantification of uncertainty in a defect-based Physics-Informed Neural Network for fatigue evaluation and insights on influencing factors. Eng Fract Mech 2023;292:109595.
[19] Tognan A, Patanè A, Laurenti L, Salvati E. A Bayesian defect-based physics-guided neural network model for probabilistic fatigue endurance limit evaluation. Comput Methods Appl Mech Eng 2024;418:116521.
[20] Wang L, Zhu S-P, Luo C, Liao D, Wang Q. Physics-guided machine learning frameworks for fatigue life prediction of AM materials. Int J Fatigue 2023;172:107658.
[21] Romano S, Brandão A, Gumpinger J, Gschweitl M, Beretta S. Qualification of AM parts: Extreme value statistics applied to tomographic measurements. Mater Des 2017;131:32–48.
[22] Tognan A, Salvati E. Probabilistic defect-based modelling of fatigue strength for incomplete datasets assisted by literature data. Int J Fatigue 2023;173:107665.
[23] E.J. Gumbel, Statistics of extremes, Columbia university press1958.
[24] Beretta S. More than 25 years of extreme value statistics for defects: Fundamentals, historical developments, recent applications. Int J Fatigue 2021;151:106407.
[25] Sordetti F, Picco N, Pelegatti M, Toninato R, Petruzzi M, Milan F, et al. Experimental Investigation of Material Characteristics that can Affect Fatigue Behaviour of Ti6Al4V Alloys Produced by Additive Manufacturing SLM and EBM Processes. Preprints: Preprints; 2026.
[26] Casagrande A, Cammarota GP, Micele L. Relationship between fatigue limit and Vickers hardness in steels. Mater Sci Eng A 2011;528(9):3468–73.
[27] Murakami Y. Effects of Hardness and Crack Geometry on ΔKthof Small Cracks. J Soc Mater Sci, Jpn 1986;35(395):911–7.
[28] Chastand V, Quaegebeur P, Maia W, Charkaluk E. Comparative study of fatigue properties of Ti-6Al-4V specimens built by electron beam melting [EBM) and selective laser melting (SLM]. Mater Charact 2018;143:76–81.
[29] Masuo H, Tanaka Y, Morokoshi S, Yagura H, Uchida T, Yamamoto Y, et al. Influence of defects, surface roughness and HIP on the fatigue strength of Ti-6Al-4V manufactured by additive manufacturing. Int J Fatigue 2018;117:163–79.
[30] Chern AH, Nandwana P, Yuan T, Kirka MM, Dehoff RR, Liaw PK, et al. A review on the fatigue behavior of Ti-6Al-4V fabricated by electron beam melting additive manufacturing. Int J Fatigue 2019;119:173–84.
[31] Le V-D, Pessard E, Morel F, Prigent S. Fatigue behaviour of additively manufactured Ti-6Al-4V alloy: the role of defects on scatter and statistical size effect. Int J Fatigue 2020;140:105811.
[32] Wu Z, Qin T, Bao J, Qian W, Salvati E, Wu S, et al. An effective approach for identifying fatigue-critical defects from X-ray 3D reconstruction: example in L-PBF AlSil0Mg alloys. Int J Fatigue 2026;206:109457.
[33] Perghem D, Salehnasab B, Beretta S, Shao S, Shamsaei N. ML-based detection of critical defects in additively manufactured parts via X-ray computed tomography. Mater Des 2025;260:115184.
[34] Rusnati L, Yosifov M, Senck S, Hubmann R, Beretta S. Anomaly detection by X-ray tomography and probabilistic fatigue assessment of aluminum brackets manufactured by PBF-LB. Mater Des 2024;248:113467.
[35] Avoledo E, Petruzzi M, Pelegatti M, Tognan A, De Bona F, Pressacco M, et al. Defect analysis by computed tomography in metallic materials: Optimisation, uncertainty quantification and classification. Precis Eng 2026;97:235–48.
[36] Barricelli L, Patriarca L, du Plessis A, Beretta S. Orientation-dependent fatigue assessment of Ti6Al4V manufactured by L-PBF: size of surface features and shielding effect. Int J Fatigue 2023;168:107401.
[37] M.M. Butt, V. Kvvssn, H. Laieghi, Z. Uddin, P. Ansari, E.K. Sadak, C.B. Toprak, H. Kızıl, E. Salvati, Characterization of Defect Distribution in an Additively Manufactured AlSi10Mg as a Function of Processing Parameters and Correlations with Extreme Value Statistics, Advanced Engineering Materials n/a(n/a) e202500641. https://advanced.onlinelibrary.wiley.com/doi/10.1002/adem.202500641.
[38] Romano S, Miccoli S, Beretta S. A new FE post-processor for probabilistic fatigue assessment in the presence of defects and its application to AM parts. Int J Fatigue 2019;125:324–41.
[39] Niu X, Zhu S-P, He J-C, Liao D, Correia JAFO, Berto F, et al. Defect tolerant fatigue assessment of AM materials: size effect and probabilistic prospects. Int J Fatigue 2022;160:106884.
[40] Forbes C, Evans M, Hastings N, Peacock B. Statistical distributions. John Wiley & Sons; 2011.
[41] Beretta S, Murakami Y. Statistical analysis of defects for fatigue strength prediction and quality control of materials. Fatigue & Fracture of Engineering Materials & Structures 1998;21(9):1049–65.
[42] Hall M, van den Boogaard HP, Fernando R, Mynett A. The construction of confidence intervals for frequency analysis using resampling techniques. Hydrol Earth Syst Sci 2004;8(2):235–46.
[43] El Haddad MH, Topper TH, Smith KN. Prediction of non propagating cracks. Eng Fract Mech 1979;11(3):573–84.
[44] Zerbst U, Bruno G, Buffière J-Y, Wegener T, Niendorf T, Wu T, et al. Damage tolerant design of additively manufactured metallic components subjected to cyclic loading: State of the art and challenges. Prog Mater Sci 2021;121:100786.
[45] Tognan A, Salvati E. B-FADE: Bayesian-fatigue model estimator in Python and its application to the probabilistic estimation of El Haddad curves. Sci Rep 2025;15(1):7106.
[46] Tarik Hasib M, Ostergaard HE, Li X, Kruzic JJ. Fatigue crack growth behavior of laser powder bed fusion additive manufactured Ti-6Al-4V: Roles of post heat treatment and build orientation. Int J Fatigue 2021;142:105955.